# Co₃O₄/Carbon Aerogel Hybrids as Anode Materials for Lithium-Ion Batteries with Enhanced Electrochemical Properties

Fengbin Hao, Zhiwei Zhang, and Longwei Yin*

Key Laboratory for Liquid−Solid Structural Evolution and Processing of Materials, Ministry of Education, School of Materials Science and Engineering, Shandong University, Jinan 250061, People's Republic of China

Ⓢ Supporting Information

ABSTRACT: A facile hydrothermal and sol−gel polymerization route was developed for large-scale fabrication of well-designed Co_3O_4 nanoparticles anchored carbon aerogel (CA) architecture hybrids as anode materials for lithium-ion batteries with improved electrochemical properties. The three-dimensional (3D) mesoporous Co_3O_4/CA hierarchical hybrids display an improved lithium storage performance and cycling stability, because of the intimate integration and strong synergistic effects between the Co_3O_4 nanoparticles and CA matrices. Such an interconnected Co_3O_4/CA hierarchical hybrid can effectively utilize the good conductivity, large surface area, 3D interconnected mesoporous structure, mechanical flexibility, chemical stability, and the short length of Li-ion transport of the CA matrix. The incorporation of Co_3O_4 nanoparticles into the interconnected CA matrix effectively reduces the number of active sites of Co_3O_4/CA hybrids, thus greatly increasing the reversible specific capacity and the initial Coulombic efficiency of the hybrids. The Co_3O_4/CA hybrid material displays the best lithium storage performance and good cycling stability as the Co_3O_4 loading content is up to 25 wt %, retains a Coulombic efficiency of 99.5% and a specific discharge capacity of 779 mAh g^{-1} after 50 cycles, 10.1 and 1.6 times larger than the specific discharge capacity of 73 mAh g^{-1} and 478 mAh g^{-1} for Co_3O_4 and CA samples, respectively. The hierarchical hybrid nanostructures with enhanced electrochemical activities using a CA matrix framework can find potential applications in the related conversion reaction electrodes.
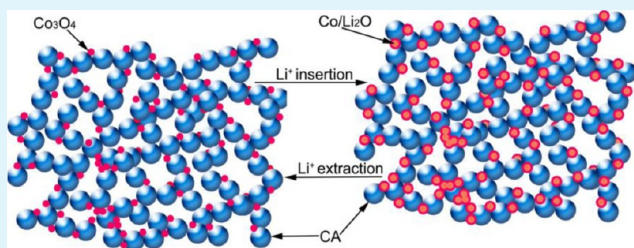
KEYWORDS: carbon aerogel, oxide, hybrid, mesoporous structure, lithium-ion battery

1. INTRODUCTION

Lithium-ion batteries (LIBs) are currently the main power source for portable electronic devices and electrical vehicles.[1−3] Graphite, as the mostly used anode material, has some disadvantages, such as low theoretical specific capacity (372 mAh g^{-1}) and low rate capability.[4] A variety of structured carbonaceous anode materials have been investigated for their applications in LIBs, such as carbon nanotubes,[5] nanofibers,[6] nanobeads,[7] hollow nanospheres,[8] graphene,[9] porous carbon,[10] and their related hybrids.[11] Carbon aerogel (CA) represents a novel and special type of porous carbon material with an interconnected structure and higher electrical conductivity than other materials.[12] CA materials, which were first reported in 1989,[13] can be fabricated via the pyrolysis of organic resorcinol−formaldehyde (RF) aqueous gels at elevated temperatures under inert atmospheres.[14,15] The main characteristics of CA materials are their large surface area (400−900 m²/g) and large pore volume (1−3 cm³/g).[16,17] Because of its controllable three-dimensional (3D) porous structure, CA is believed to be an ideal electrode material for supercapacitors and rechargeable batteries, because of their mesoporous interconnected structure, high specific surface area, abundant micropores and mesopores, and good electric conductivity.[18,19]

Co_3O_4 has attracted extensive interest for LIBs, because of its large theoretical capacity (890 mAh g^{-1}), which is much larger than that of graphite (372 mAh g^{-1}).[20−22] However, a large amount of volume expansion/contraction and severe particle aggregation may be generated during the lithiation and delithiation process: the electrode pulverization and loss of interparticle contact will cause a large irreversible capacity loss and poor cycling stability.[23,24] To further enhance the electrochemical properties of Co_3O_4 electrodes, the key to utilizing it to a fuller extent is to design the microstructure of Co_3O_4 as an anode material.[18,23,24] An effective route is to construct a hybrid with Co_3O_4 nanoparticles incorporated in a porous matrix with good conductivity. A variety of techniques have been attempted to solve these intractable problems, including carbon-based nanohybrids[24−27] and uniquely designed Co_3O_4 nanostructures/microstructures of nanotubes,[15] nanowires,[22] nanoparticles (NPs),[28] nanosheets,[29] octahedral cages.[30]

Metal oxide/carbon hybrids can present synergistic or cooperation effects between the metal oxide and the carbon

phase.[31,32] It is expected that this effect would be enhanced if the Co_3O_4 nanoparticles are well-dispersed onto the carbon matrices. The special structure and high surface area of CA materials should be a good carrier for Co_3O_4 nanoparticales, which can buffer its large volume expansion/contraction. Furthermore, to optimize the properties of CA materials for specific applications in LIBs and supercapcitors, recent efforts have been focused on the functionalization of the CA framework, either through modification of the aerogel surface or through incorporation of the additives, such as oxide nanoparticles, into the framework structure. The strategy is to expose as much of the active material as possible to the electrolyte, so that the superficial redox reactions can proceed to a fuller extent.

Here, we report a facile strategy to synthesize Co_3O_4/CA architectural hybrids with Co_3O_4 nanoparticles homogenously distributed in the pore channels of CA matrix. The as-prepared Co_3O_4 nanoparticle intercalated mesoporous CA matrices represents a typical connected hierarchical nanostructure, in which CA plays the roles of both an electronically conductive network and an elastic buffer for the Co_3O_4 nanoparticles.[33−35] Cyclic voltammetry (CV) and galvanostatic capability characterization was carried out to evaluate the electrochemical behaviors and lithium storage performance of the Co_3O_4/CA hybrids. It is shown that the 25% Co_3O_4/CA hybrid displays an initial columbic efficiency of 50.4% and excellent electrochemical cycling stability, corresponding to a columbic efficiency of 99.5% at 50 cycles, retaining an improved specific discharge capacity of 779 mAh g^{-1}, which is 10.1 and 1.6 times larger than the specific discharge capacity of 73 mAh g^{-1} and 478 mAh g^{-1} for the Co_3O_4 and CA samples, respectively.

2. EXPERIMENTAL SECTION

2.1. Preparation of the CA and Co_3O_4/CA Hybrids. For the typical synthesis of CA materials,[36] 5.5 g of resorcinol (R) and 8.1 g of formaldehyde (F) (37 wt %) were added to 14.75 g H_2O (the RF weight percentage was ~30 wt %), the mixture was stirred for 10 min. Then, a certain amount of sodium carbonate catalyst (C) was added to the above solution, with a RC ratio of 500, 1000, and 1500. After 20 min continuously stirring, the mixture was transferred to a flat-bottom flask. The samples were then treated in a (1,1,1) cycle, where the numbers stand for the number of days at room temperature, 50 °C, and 90 °C, respectively. All the RF gels were dried under ambient conditions. A pyrolysis route was applied to transform the gels to carbon aerogels at 1000 °C with a heating rate of 3 °C min^{-1} and kept for 2 h under a protective nitrogen gas atmosphere.

Scheme 1 depicts a model for the fabrication process of Co_3O_4/CA hybrids. The Co_3O_4/CA hybrids with different contents of Co_3O_4 (15,
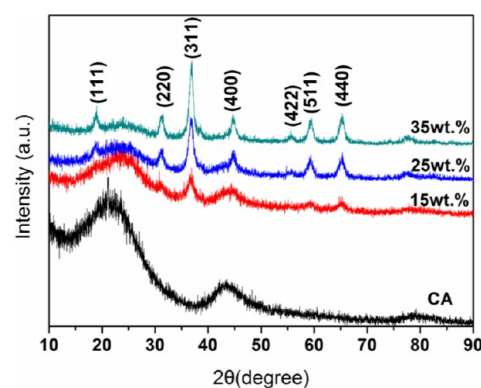
Scheme 1. Illustration of the Fabrication Process of Co_3O_4/CA Hybrids

25, and 35 wt %) were prepared as follows. A certain amount of $Co(NO_3)_2 \cdot 6H_2O$ was dispersed into a small amount of water, and then 0.5 g of CA (RC = 500) was added to the above solution. The mixture then was stirred for 12 h and dried at 60 °C. Finally, the mixture of CA and $Co(NO_3)_2 \cdot 6H_2O$ was heated up to 300 °C in a tube furnace and kept for 5 h under a protecting nitrogen gas flow. For the comparison of lithium storage performances between the Co_3O_4/CA and pure Co_3O_4 samples, the pure Co_3O_4 samples were prepared by directly calcining $Co(NO_3)_2 \cdot 6H_2O$ in a tube furnace.

2.2. Sample Characterization. The powder X-ray diffraction (XRD) patterns of the products were determined by a Rigaku D/Max-KA diffractometer that was equipped for Cu Kα radiation. The morphology and chemical components of the products were analyzed using a field-emission scanning electron microscopy (FE-SEM) system (Hitachi, Model SU-70). The microstructures of the synthesized products were analyzed using a high-resolution transmission electron microscopy (HR-TEM) system (JEOL, Model JEM-2100) at an acceleration voltage of 200 kV.[37,38] Nitrogen adsorption−desorption isotherms were determined at 77 K, using a Micromeritics Model ASAP 2020 surface area and porosity analyzer, as reported in our previous work.[39] The surface area measurements were performed according to the Brunauer−Emmett−Teller (BET) method. The pore size distribution was obtained from the desorption branch of the isotherm, using the corrected form of Kelvin equation by means of the Barrett−Joyner−Halenda (BJH) method. Raman spectra were measured and collected using a 632.8-nm laser with a Raman spectrometer (Jobin−Yvon, Model JY HR800) under ambient conditions, with a laser spot size of ~1 μm.

2.3. Electrochemical Measurements. Working electrodes were prepared by mixing 80 wt % the CA or Co_3O_4/CA material, 10 wt % acetylene black (Super-P), and 10 wt % poly(vinylidene fluoride) binder dissolved in N-methyl-2-pyrrolidinone. The galvanostatic charging/discharging test is the same as previously reported.[37,38] It was conducted using standard 2032 type coin cells with copper foil as the current collector, lithium foil as reference electrodes, and 1.0 M LiPF$_6$ in mixed ethylene carbonate (EC) and diethyl carbonate (DEC) (EC:DEC, 1:1 by volume) as the electrolyte. A cutoff voltage window of 0.01−3.0 V was used. The standard 2032 coin-type cells were assembled in an argon-filled glovebox with <1 ppm of oxygen and water, galvanostatically cycled on a LAND CT2001A instrument (Wuhan Jinnuo Electronics, Ltd., Wuhan, China) at room temperature. A cyclic voltammetry (CV) study was conducted using an electrochemical workstation (Princeton Applied Research, Model PARSTAT 2273) between 0.01 V and 3.0 V at a scan rate of 0.1 mV s^{-1}.
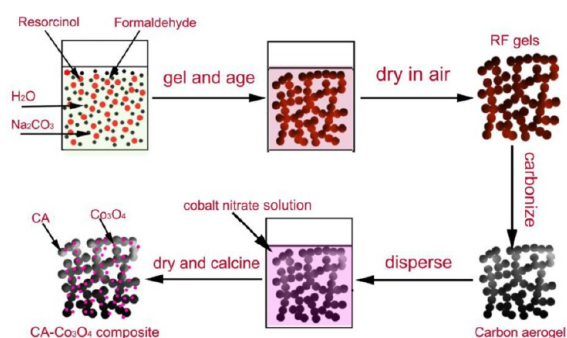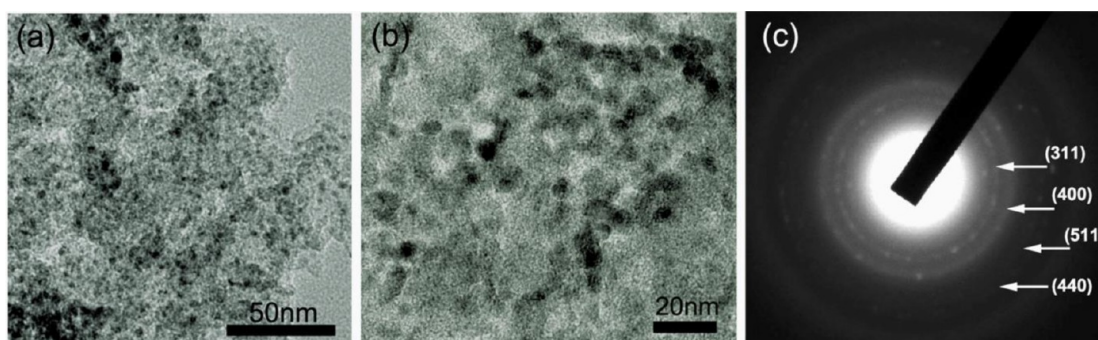
3. RESULTS AND DISCUSSION

Figure 1 depicts XRD patterns of the synthesized Co_3O_4/CA hybrid samples. The (111), (220), (311), (400), (422), (511),

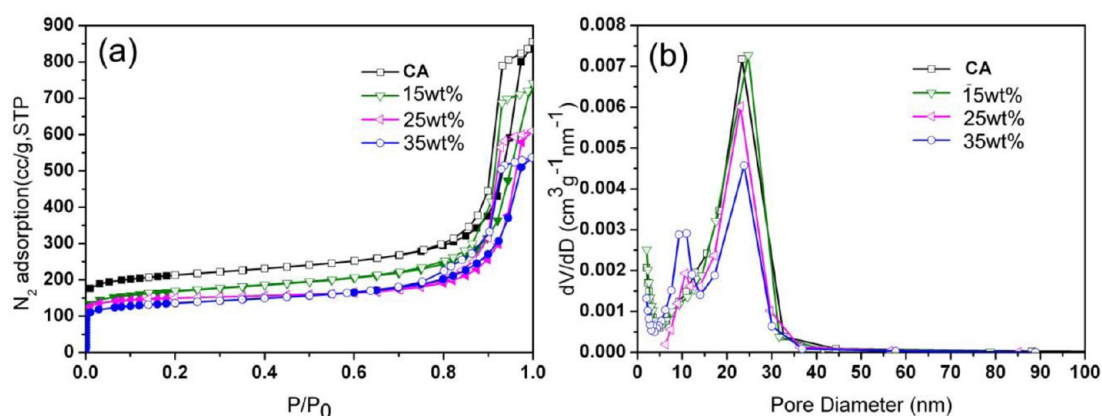**Figure 1.** X-ray diffraction (XRD) patterns for CA and Co_3O_4/CA composites with different contents of Co_3O_4 nanoparticles incorporated.

Figure 2. (a,b) High-magnification transmission electron microscopy (TEM) images of Co_3O_4/CA composites. (c) Selected-area electron diffraction (SAED) pattern of the Co_3O_4 nanoparticles.

Figure 3. (a) N_2 adsorption−desorption isotherms of CA and Co_3O_4/CA hybrids (closed symbols represent adsorption data; open symbols represent desorption data). (b) Pore size distributions of CA and Co_3O_4/CA hybrids.

and (440) peaks in the XRD patterns match well with that of face-centered cubic Co_3O_4 with a lattice constant of $a = 0.808$ nm (fcc, $Fd3m$, JCPDS No. 42-1467). The additional broad and small (002) and (100) diffraction peaks appearing at $2\theta = 22°$ and 44° can be indexed to the amorphous carbon of CA matrices. No other peaks appeared, indicating that the synthesized products are composed of amorphous carbon and cobalt oxide (Co_3O_4). For the pure XRD pattern of pure CA samples, it shows a typical amorphous carbon structure with the peaks centered at ~22° and 44° (see Figure S1 in the Supporting Information).
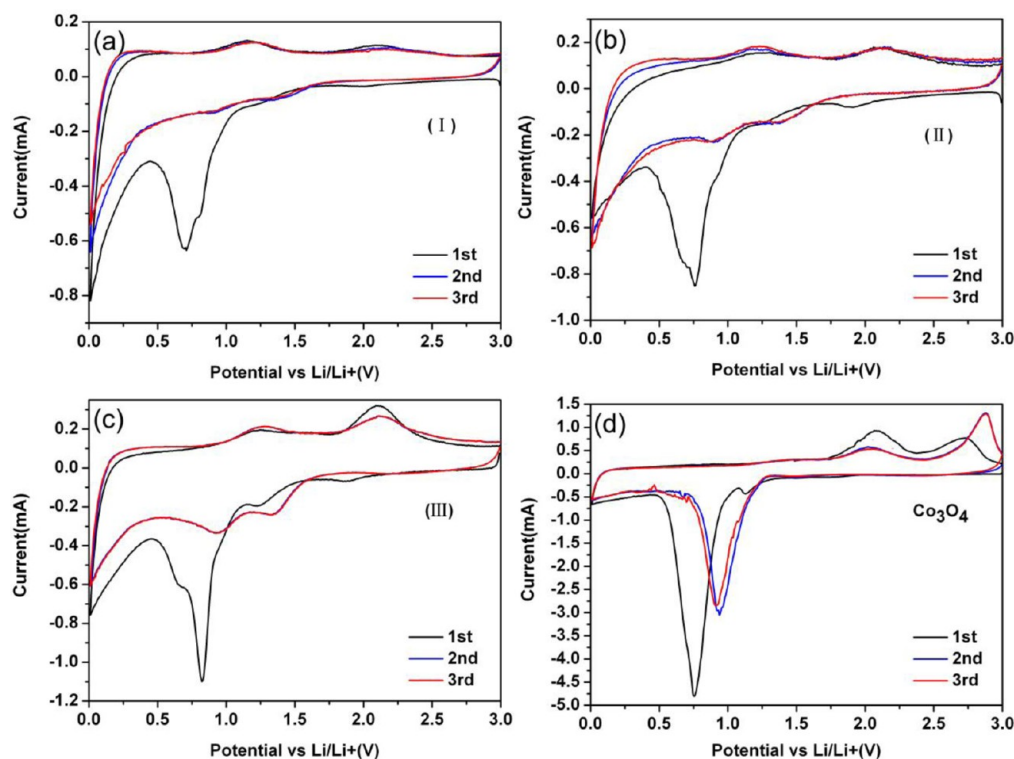
The microstructures of the CA materials were observed via FE-SEM and HR-TEM, as shown in Figure S3 of the Supporting Information. The CA materials are composed of carbon spheres interconnecting each other, forming a 3D network architectural structure. The particle size of CA increases as the RC ratio increases: the particle sizes of RC = 1000 and 1500 are ~200 nm and ~2 μm, respectively, while the particle size is ~20 nm for RC = 500. Figure 2a depicts a typical TEM image of the 25%Co_3O_4/CA hybrid. It is clearly illustrated from Figure 2a that the distribution and dimension of the Co_3O_4 nanoparticles are homogeneous. The diameter of the Co_3O_4 nanoparticles is ~5 nm. Figure 2c is a typical selected-area electron diffraction (SAED) pattern of the Co_3O_4 nanoparticles, the diffraction rings correspond to (311), (400), (511), and (440) planes of face-centered cubic Co_3O_4 (space group: $Fd\overline{3}m$) with lattice constants of $a = 0.808$ nm. From a HRTEM lattice image of single Co_3O_4 nanoparticle (see Figure S4 in the Supporting Information), it is shown that the marked d-spacing of 0.20 nm is consistent with that of the (400) planes

of face-centered cubic Co_3O_4 (space group: $Fd\overline{3}m$) with lattice constants of $a = 0.808$ nm.

The Brunauer−Emmett−Teller (BET) specific surface area and porous characteristics of the Co_3O_4/CA hybrid samples with different incorporated Co_3O_4 contents were investigated by nitrogen adsorption−desorption isotherms. The nitrogen adsorption−desorption isotherms and pore size distribution of the Co_3O_4/CA hybrids with different Co_3O_4 contents are shown in Figure 3. All the samples exhibit typical Type IV isotherms with a H_1 hysteresis loop with a similar curve, indicating a disordered mesoporous structure for the Co_3O_4/CA hybrids. The BET specific surface area, pore diameter, total pore volume, and micropore volume of Co_3O_4/CA hybrids are listed in Table 1. As shown in Table 1, the BET surface area of Co_3O_4/CA hybrids decreases as the Co_3O_4 content increases, and the surface area of CA sample is 669 m^2 g^{-1}; as the Co_3O_4

Table 1. Textural Parameters of the Co_3O_4/CA Hybrids

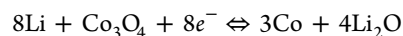| sample	BET surface area (m^2 g^{-1})	pore diameter (nm)	total pore volume (cm^3 g^{-1})	micropore volume (cm^3 g^{-1})
CA	669	11.8	1.12	0.22
15% Co_3O_4/ CA	533	15.9	1.01	0.14
25% Co_3O_4/ CA	459	15.2	0.944	0.13
35% Co_3O_4/ CA	429	14.6	0.83	0.11

Figure 4. Cyclic voltammometric (CV) curves of the first three cycles for Co_3O_4/CA hybrids: (a) 15%Co_3O_4, (b) 25%Co_3O_4, (c) 35%Co_3O_4, and (d) pure Co_3O_4. All scans performed at a scan rate of 0.1 mV s^{-1} between 0.01 V and 3.0 V.

incorporated contents increase, the surface area of the synthesized hybrids decreases from 533 m^2 g^{-1} for the 15% Co_3O_4/CA sample to 429 m^2 g^{-1} for the 35%Co_3O_4/CA sample. The average pore diameter of Co_3O_4/CA hybrids display a trend similar to that of the BET surface area: the average pore diameter of Co_3O_4/CA hybrids changes from 11.8 nm for pure CA, to 15.9 nm for the 15%Co_3O_4/CA sample, to 15.2 nm for the 25%Co_3O_4/CA hybrid. The reason for the average pore diameter of the Co_3O_4/CA sample being larger than that of the pure CA sample is that micropores <2 nm in size are blocked, because of the incorporation of Co_3O_4 nanoparticles, with larger mesopores (2−50 nm) being left behind. However, as the Co_3O_4 content increases, some of the mesopores are also blocked, so the average pore diameter of Co_3O_4/CA sample displays a slightly decreasing trend. The total pore volume decreases from 1.12 cm^3 g^{-1} for the 15% Co_3O_4/CA hybrid sample to 0.83 cm^3 g^{-1} for the 35% Co_3O_4/CA hybrid sample. The nitrogen adsorption−desorption isotherms and pore size distribution of CA are shown in Figure S2 in the Supporting Information. The BET specific surface area, pore diameter, total pore volume, and micropore volume of CA are listed in Table S1 in the Supporting Information.

The cyclic voltammogram (CV) curves of the Co_3O_4/CA samples were used to understand the electrochemical process of the lithiation and delithiation of the hybrids. Figures 4a, 4b, and 4c depict CV curves of the Co_3O_4/CA samples with different contents of incorporated Co_3O_4 (15, 25, and 35 wt %, respectively). As shown in Figures 4a−c, a cathodic peak at ~0.7−0.8 V appears in the first cycle curve for the Co_3O_4/CA hybrids with different Co_3O_4 contents, corresponding to the initial reduction process of Co_3O_4 to metallic cobalt, the electrochemical formation of amorphous Li_2O, and a

passivating solid electrolyte interface (SEI) film.[35,36] As the Co_3O_4 content in the Co_3O_4/CA samples increases, the cathodic peak shifts to a relatively large potential position, from a position at 0.61 V for pure CA sample to positions of 0.7, 0.75, and 0.8 V for the 15, 25, and 35 wt % Co_3O_4-incorporated Co_3O_4/CA samples. Furthermore, the peak intensity of the cathodic current becomes stronger as the Co_3O_4 content increases (from 0.5 mA g^{-1} to 1.1 mA g^{-1}), revealing a fast kinetics process for the phase transformation of Co_3O_4 and the formation of the SEI film.[22]

It has been shown from the above TEM analysis that the grain size of the Co_3O_4 nanoparticles in the Co_3O_4/CA hybrids is fine (~5 nm), and the specific surface area is large, so the electrochemical process related to the lithiation and delithiation reactions is relatively severe, which results in a higher cathodic current in the first cycle. During the subsequent anodic scan, there exists a broad peak located at ~2.15 V, which can be attributed to the oxidation reaction and formation of cobalt oxide. From the second cycle, the main reduction peak shifts to 0.9 V and the peak intensity apparently decreases, whereas the peak at 2.15 V displays very little modification. In addition, the peak intensity and integral area at the third cycle are very similar to those at the second cycle, suggesting a high reversibility of electrochemical reaction. The conversion reaction associated with these processes can be described as[39−43]

$$8Li + Co_3O_4 + 8e^- \Leftrightarrow 3Co + 4Li_2O$$

$$8Li \Leftrightarrow 8Li^+ + 8e^-$$

$$Co_3O_4 + 8Li \Leftrightarrow 3Co + 4Li_2O$$

A galvanostatic technique was utilized to investigate the charge−discharge cycling performance of the mesoporous
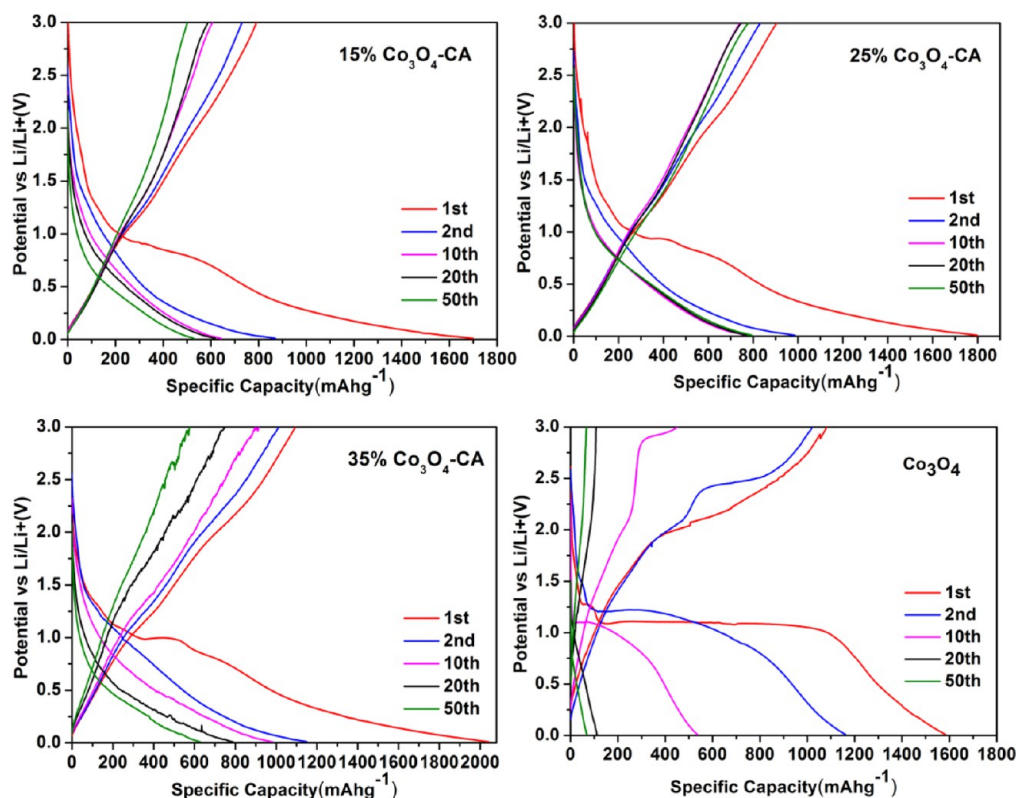
Figure 5. Electrochemical performances of Co_3O_4/CA hybrids and pure Co_3O_4: the 1st, 2nd, 10th, 20th, and 50th charge−discharge curves between 0.01 V and 3 V at a current of 50 mA g^{-1} for (a) 15%Co_3O_4/CA, (b) 25%Co_3O_4/CA, (c) 35%Co_3O_4/CA, and (d) pure Co_3O_4.
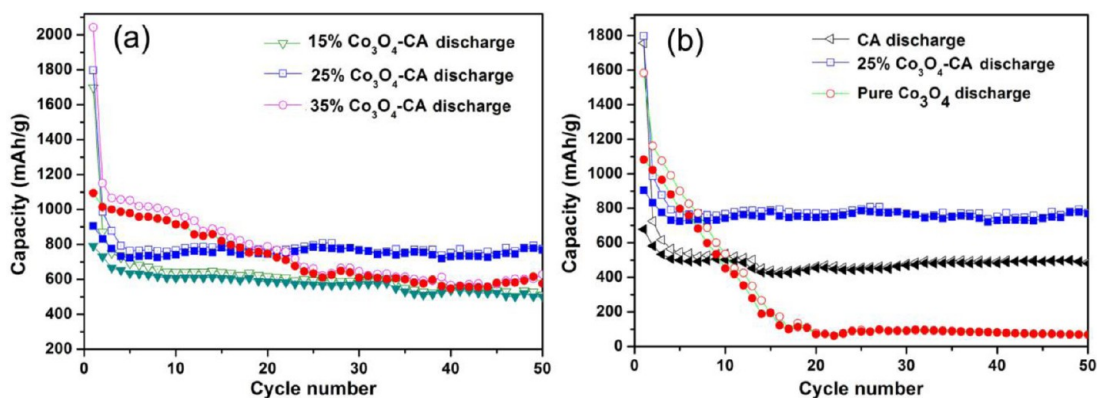
Figure 6. (a,b) Capacity versus cycle number curves of Co_3O_4/CA hybrids, CA (RC = 500), pure Co_3O_4, between 0.01 V and 3 V at the discharge current of 50 mA g^{-1}.

Co_3O_4/CA hybrids. Figures 5a−c depict the 1st, 2nd, 10th, 20th, and 50th discharge/charge voltage profiles of the synthesized Co_3O_4/CA hybrids (15, 25, and 35 wt % Co_3O_4, respectively) and pure Co_3O_4 sample at a current density of 50 mA g^{-1} between 0.01 V and 3 V at room temperature. It is clearly shown that, as the Co_3O_4-incorporated content in the CA matrices increases, both the discharge capacity and charge capacity greatly increase. The Co_3O_4/CA hybrid samples display a discharge capacity of 1698, 1797, and 2043 mAh g^{-1}, and a charge capacity of 798, 905, and 1089 mAh g^{-1}, and the irreversible capacity is 900, 892, and 954 mAh g^{-1} (corresponding to 15, 25, and 35 wt % Co_3O_4, respectively), in the first cycle, showing the improved performance and superiority of the Co_3O_4/CA hybrids, compared to that of pure Co_3O_4 and the pure CA sample (RC = 500, first Coulombic

efficiency = 38.6%). The pure Co_3O_4 sample (data shown in Figure 5d) shows a discharge capacity of 1584 mAh g^{-1} and a charge capacity of 1087 mAh g^{-1} in the first cycle.

In the following 2nd, 10th, 20th, and 50th cycles, as the Co_3O_4 nanoparticle contents incorporated in the CA matrices increase, the lithium capacity first increases and then decreases quickly as the content of Co_3O_4 is reaches a value of 35 wt %. At the 2nd cycle, the discharge capacity of Co_3O_4/CA hybrids is 875, 987, and 1154 mAh g^{-1} (15, 25, and 35 wt % Co_3O_4, respectively). At the 20th cycle, the discharge capacity of Co_3O_4/CA hybrids is 627, 777, and 793 mAh g^{-1}. While at the 50th cycle, the discharge capacity of Co_3O_4/CA hybrids can still retain at 524, 779, and 629 mAh g^{-1} (15, 25, and 35 wt % Co_3O_4), respectively. For pure Co_3O_4 sample, the discharge

capacity at the 2nd, 20th, and 50th cycle is 1025, 106, and 73 mAh g^{-1}, respectively.

From Figure 5, it is indicated that, for the pure Co_3O_4 sample, it presents a long voltage plateau at 1.10 V in the first discharge step, followed by a declining curve to an end voltage of 0.01 V, which is a character for the pure Co_3O_4 sample.[21] For the Co_3O_4/CA hybrids, as the content of Co_3O_4 is low, the Co_3O_4/CA hybrid does not show an apparent long voltage plateau in the first discharge step. As the content of Co_3O_4 increases, the voltage plateau at 1.00 V is more and more apparent in the first discharge step, as shown in the first discharge profile of 35% Co_3O_4/CA hybrid sample in Figure 5.

Figure 6 comparatively depicts the lithium storage performance and the cycling stability of Co_3O_4/CA composites with different Co_3O_4 mass loading, CA (RC = 500) and pure Co_3O_4 at a galvanostatic charge/discharge current of 50 mAh g^{-1} between 0.01 V and 3.0 V (vs Li$^+$/Li). Figure 6a indicates that, as the Co_3O_4 content increases, both the discharge capacity and charge capacity of Co_3O_4/CA hybrids greatly increase. The Co_3O_4/CA hybrid samples display an initial discharge capacity of 1698, 1797, and 2043 mAh g^{-1}, and an initial Coulombic efficiency of 46.5%, 50.4%, and 53.6% (15, 25, and 35 wt % Co_3O_4, respectively), as shown in Figure 7 for the Coulombic
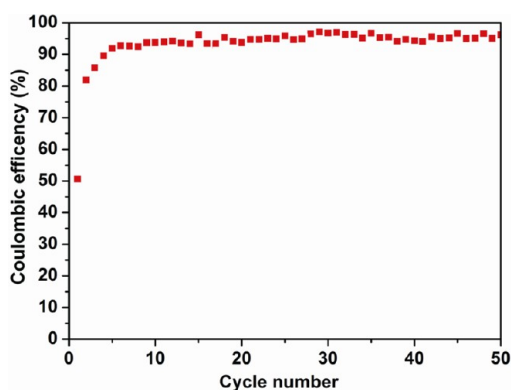
**Figure 7.** Coulombic efficiency for the 25%Co_3O_4/CA hybrid sample.

efficiency of the 25%Co_3O_4/CA hybrid sample. The Co_3O_4/CA hybrid materials exhibit good cycling stability when the Co_3O_4 mass load is up to 25 wt %. Even after the 50th cycle, the 25%Co_3O_4/CA sample still retains a discharge capacity of 779 mAh g^{-1} and a charge capacity of 774 mAh g^{-1}, corresponding to a Coulombic efficiency of 99.5%. Although the 35%Co_3O_4/CA sample shows the best initial discharge capacity of 2043 mAh g^{-1} and charge capacity of 1098 mAh g^{-1}, corresponding to an initial Coulombic efficiency of 53.6%, it cannot retain a high value of specific capacity in the following cycles. During the first 25 cycles, the capacity decreases drastically as the number of cycles increases, with the discharge capacity decreasing from a value of 1159 mAh g^{-1} at the 2nd cycle to 661 mAh g^{-1} at the 25th cycle. After 50 cycles, the 35% Co_3O_4/CA sample only remains at a specific discharge capacity of 623 mAh g^{-1}. This is because an excess addition of Co_3O_4 nanoparticles may destroy the mesoporous structure and block the pore channels of the CA matrices, which is disadvantageous to Li$^+$ transfer. For the 15%Co_3O_4/CA sample, after 50 cycles, the discharge capacity decreases from a value of 1699 mAh g^{-1} at the 1st cycle to 502 mAh g^{-1}.

Figure 6b shows that the pure CA sample displays an initial discharge capacity of 1753 mAh g^{-1} and an initial charge

capacity of 680 mAh g^{-1}, with an irreversible capacity of 1073 mAh g^{-1}, corresponding to an initial Coulombic efficiency of 38.7%. At the 50th cycle, the discharge capacity only retains at a value of 478 mAh g^{-1}. Furthermore, the Coulombic efficiency at the first 10 cycle is relatively low, displaying a high value of irreversible capacity.

For the pure Co_3O_4 sample (Figure 6b), it displays the discharge capacity of 1584 mAh g^{-1} and a charge capacity of 1087 mAh g^{-1} in the first cycle, corresponding to a Coulombic efficiency of 68.3%. Although the initial Coulombic efficiency is relatively high, the capacity decreases quickly as the number of cycles increases. From the 2nd cycle to the 15th cycle, the capacity decreases gradually as the number of cycles increases. After 20 cycles, the discharge capacity can only maintain a value of 77 mAh g^{-1}. The discharge capacity of pure Co_3O_4 sample at the 50th cycle can only retain a value of 73 mAh g^{-1}.

Figure 8 shows a schematic of the insertion/extraction process of the mesoporous, interconnected 3D Co_3O_4/CA
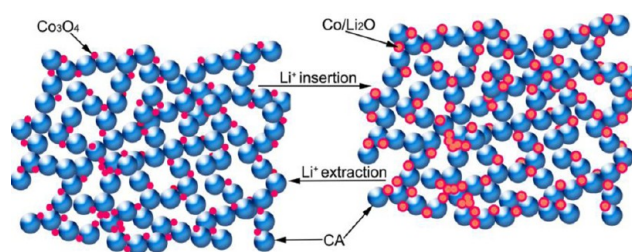
Figure 8. Schematic diagram of the insertion/extraction process of the mesoporous interconnected three-dimensional (3D) Co_3O_4/CA hybrids.

hybrids. In the Li$^+$ insertion/extraction process, Co_3O_4 + 8Li → 4Li$_2$O + 3Co, as reported previously,[23,24] a large volume expansion/contraction of ∼300% occurs. The improved lithium storage performance and cycling stability of the mesoporous Co_3O_4/CA hierarchical hybrids are attributed to the intimate integration and strong synergistic effects between the Co_3O_4 nanoparticles and CA matrices. In general, such a 3D interconnected Co_3O_4/CA hierarchical hybrid can effectively utilize the good conductivity, large surface area, 3D interconnected mesoporous structure, mechanical flexibility, chemical stability, and short length of Li ion transport of the CA matrix.

(1) The incorporation of Co_3O_4 nanoparticles in the 3D connected CA effectively reduces the number of active sites of CA matrices; thus, the irreversible capacity of hybrids can be greatly reduced. For the Co_3O_4/CA hierarchical hybrid samples, Co_3O_4 nanocrystals can offer active sites for reversible reactions, and the interconnected mesoporous CA matrix provides several Li-storage sites.[44] According to the above electrochemical performance analysis, the synthesized Co_3O_4/CA hybrid samples display initial Coulombic efficiencies of 46.5%, 50.4%, and 53.6% for the 15%, 25%, and 35% Co_3O_4-incorporated Co_3O_4/CA hybrid samples, respectively. The CA sample displays a low initial Coulombic efficiency of 38.7% , because of the large irreversible capacity.

(2) The 3D networked CA in the Co_3O_4/CA hybrid samples serves as an efficient electric matrix for Co_3O_4 nanoparticle homogeneous dispersion. The electron transfer ability of the Co_3O_4/CA hybrid can be greatly improved by combining Co_3O_4 with a CA matrix with good conductivity. The mesostructure of the 3D mesoporous CA provides enough

space for Li$^+$ storage and greatly reduces charge-transfer paths. The CA matrices with good electrical conductivity can effectively decrease the charge-transfer resistance, improving the specific capacity of LIBs.[35]

(3) The 3D interconnected CA can work as buffers to alleviate the strain of Co_3O_4 nanoparticles during the lithiation and delithiation process. CA matrices with Co_3O_4 nanoparticles homogenously dispersed can effectively prevent the aggregation of the ultrafine Co_3O_4 nanoparticles. The mesoporous CA matrices in the Co_3O_4/CA hybrids can moderate the strain and stress of Co_3O_4 NPs during the lithiation and delithiation process, and inhibit the aggregation of Co_3O_4 NPs and pulverization of the electrode materials upon continuous cycling, thus displaying a high specific capacity, a high Coulombic efficiency, and a high rate capability and cycling stability.

(4) The diffusion of Li-ion and charge transfer ability are mainly dependent on the transport length and accessible sites on the surface of active materials. The small size and homogeneous distribution of Co_3O_4 nanoparticles in CA matrices is very useful for the alleviation of the large strain and stress during the lithiation and delithiation process. The larger electrochemical active surface area of CA and/or grain boundary area of the Co_3O_4 nanoparticles also contribute to the extra discharge capacity of the Co_3O_4/CA hybrids.

4. CONCLUSIONS

We report a facile hydrothermal and sol−gel polymerization route to develop large-scale fabrication of well-designed Co_3O_4 nanoparticles (NPs) anchored carbon aerogel (CA) architecture hybrids as anode materials for lithium-ion batteries (LIBs) with improved electrochemical property. The effects of different content loadings of Co_3O_4 NPs on the microstructures, surface area, pore diameter, and pore volume of the mesoporous Co_3O_4/CA hybrids were investigated using X-ray diffraction (XRD), nitrogen sorption, thermogravimetric analysis (TGA), field-emission scanning electron microscopy (FE-SEM), and high-resolution transmission electron microscopy (HR-TEM). Cyclic voltammetry (CV) and galvanostatic capability characterization were carried out to evaluate the electrochemical performance of the Co_3O_4/CA composites. The Co_3O_4/CA hybrid materials displays the best lithium storage performance and good cycling stability as the Co_3O_4 loading content increases up to 25 wt %, retaining a discharge capacity of 779 mAh g^{-1} and a charge capacity of 774 mAh g^{-1} after the 50th cycle, corresponding to a Coulombic efficiency of up to 99.5%. The improved electrochemical performance and cycling stability of the mesoporous Co_3O_4/CA hierarchical hybrids are due to the intimate integration and strong synergistic effects between the Co_3O_4 NPs and CA matrices. The incorporation of Co_3O_4 NPs in the interconnected Co_3O_4/CA hierarchical hybrids reduces the number of active sites of CA matrices, thus greatly increasing the reversible specific capacity of the hybrids and the first Coulombic efficiency. The as-prepared Co_3O_4 NPs intercalated in porous channels of CA matrices form a typical hierarchical nanostructure, in which CA plays the roles of both an electronically conductive network and an elastic buffer for the Co_3O_4 NPs. The mesoporous structure of CA provide a buffer architecture for the stress and strain of Co_3O_4 NPs during the lithiation and delithiation process. The high porosity and three-dimensional (3D) interconnected mesopore structure of CA provides essential channels for charge transport. The Co_3O_4/CA hybrids via an economically

feasible synthetic route with excellent electrochemical performance could find potential applications as anode materials for LIBs.

■ ASSOCIATED CONTENT

Ⓢ Supporting Information

Electronic Supporting Information (ESI) available: XRD patterns and FE-SEM images of CA samples, TGA curve of the Co_3O_4−CA hybrids under air, Raman spectra of the CA, cyclic voltammetric curves of the first three cycles for CA, andn electrochemical performances and impedance spectra of CA samples. This material is available free of charge via the Internet at http://pubs.acs.org.

■ AUTHOR INFORMATION

Corresponding Author

*Tel.: +86 531 88396970. Fax: +86 531 88396970. E-mail: yinlw@sdu.edu.cn.

Notes

The authors declare no competing financial interest.

■ ACKNOWLEDGMENTS

■ REFERENCES

(1) Tarascon, J. M.; Armand, M. *Nature* **2001**, *414*, 359−367.
(2) Goodenough, J. B.; Kim, Y. *Chem. Mater.* **2010**, *22*, 587−603.
(3) Armand, M.; Tarascon, J. M. *Nature* **2008**, *451*, 652−657.
(4) Guo, B.; Wang, X.; Fulvio, P. F.; Chi, M.; Mahurin, S. M.; Sun, X.-G.; Dai, S. *Adv. Mater.* **2011**, *23*, 4661−4664.
(5) Landi, B. J.; Ganter, M. J.; Cress, C. D.; DiLeo, R. A.; Raffaelle, R. P. *Energy Environ. Sci.* **2009**, *2*, 638−654.
(6) Li, C.; Yin, X.; Chen, L.; Li, Q.; Wang, T. *J. Phys. Chem. C* **2009**, *113*, 13438−13422.
(7) Wang, H.; Abe, T.; Maruyama, S.; Iriyama, Y.; Ogumi, Z.; Yoshikawa, K. *Adv. Mater.* **2005**, *17*, 2857−2859.
(8) Han, F.-D.; Bai, Y.-J.; Liu, R.; Yao, B.; Qi, Y.-X.; Lun, N.; Zhang, J.-X. *Adv. Energy Mater.* **2011**, *1*, 798−801.
(9) Wu, Z.-S.; Ren, W.; Xu, L.; Li, F.; Cheng, H.-M. *ACS Nano* **2011**, *5*, 5463−5471.
(10) Lee, K. T.; Lytle, J. C.; Ergang, N. S.; Oh, S. M.; Stein, A. *Adv. Funct. Mater.* **2005**, *15*, 547−556.
(11) Zhang, J.; Hu, Y.-S.; Tessonnier, J.-P.; Weinberg, G.; Maier, J.; Schlögl, R.; Su, D. S. *Adv. Mater.* **2008**, *20*, 1450−1455.
(12) Lu, X.; Nilsson, O.; Fricke, J.; Pekala, R. W. *J. Appl. Phys.* **1993**, *73*, 581−584.
(13) Pekala, R. W. *J. Mater. Sci.* **1989**, *24*, 3221−3237.
(14) Reynolds, G. A. M.; Fung, A. W. P.; Wang, Z. H.; Dresselhaus, M. S.; Pekala, R. W. *J. Non-Cryst. Solids* **1995**, *188*, 27−33.
(15) Al-Muhtaseb, S. A.; Ritter, J. A. *Adv. Mater.* **2003**, *15*, 101−114.
(16) Hanzawa, Y.; Kaneko, K.; Pekala, R. W.; Dresselhaus, M. S. *Langmuir* **1996**, *12*, 6167−6175.
(17) Wu, D.; Sun, Z.; Fu, R. *J. Appl. Polym. Sci.* **2006**, *99*, 2263−2267.
(18) Shen, J.; Hou, J.; Guo, Y.; Xue, H.; Wu, G.; Zhou, B. *J. Sol−Gel Sci. Technol.* **2005**, *36*, 131−136.
(19) Wang, J.; Zhang, S. Q.; Shen, J.; Guo, Y. Z.; Attia, S. M.; Zhou, B.; Lai, Z. Q.; Zheng, G. Z.; Gui, Y. S. *J. Porous Mater.* **2001**, *8*, 167−170.

(20) Du, N.; Zhang, H.; Chen, B. D.; Wu, J. B.; Ma, X. Y.; Liu, Z. H.; Zhang, Y. Q.; Yang, D. R.; Huang, X. H.; Tu, J. P. *Adv. Mater.* **2007**, *19*, 4505−4509.

(21) Yao, W.; Yang, J.; Wang, J.; Nuli, Y. *J. Electrochem. Soc.* **2008**, *155*, A903−A908.

(22) Li, W. Y.; Xu, L. N.; Chen, J. *Adv. Funct. Mater.* **2005**, *15*, 851−857.

(23) Li, Y.; Tan, B.; Wu, Y. *Nano Lett.* **2008**, *8*, 265−270.

(24) Yao, W.-L.; Wang, J.-L.; Yang, J.; Du, G.-D. *J. Power Sources* **2008**, *176*, 369−372.

(25) Yao, W.; Yang, J.; Wang, J.; Tao, L. *Electrochim. Acta* **2008**, *53*, 7326−7330.

(26) Zhi, L.; Hu, Y.-S.; Hamaoui, B. E.; Wang, X.; Lieberwirth, I.; Kolb, U.; Maier, J.; Müllen, K. *Adv. Mater.* **2008**, *20*, 1727−1731.

(27) Liu, H. J.; Bo, S.-h.; Cui, W.-j.; Li, F.; Wang, C.-x.; Xia, Y.-y. *Electrochim. Acta* **2008**, *53*, 6497−6503.

(28) Liu, B.; Zhang, X.; Shioyama, H.; Mukai, T.; Sakai, T.; Xu, Q. *J. Power Sources* **2010**, *195*, 857−861.

(29) Zhan, F.; Geng, B.; Guo, Y. *Chem.—Eur. J.* **2009**, *15*, 6169−6174.

(30) Wang, X.; Yu, L.; Wu, X.-L.; Yuan, F.; Guo, Y.-G.; Ma, Y.; Yao, J. *J. Phys. Chem. C* **2009**, *113*, 15553−15558.

(31) Yang, X. L.; Fan, K. C.; Zhu, Y. H.; Shen, J. H.; Jiang, X.; Zhao, P.; Li, Ch.-zh. *J. Mater. Chem.* **2012**, *22*, 17278−17283.

(32) Yang, X. L.; Fan, K.-c.; Zhu, Y.-h.; Shen, J.-h.; Jiang, X.; Zhao, P.; Luan, S. R.; Li, C. Z. *ACS Appl. Mater. Interfaces* **2013**, *5*, 997−1002.

(33) Li, G. R.; Feng, Z. P.; Ou, Y. N.; Wu, D. C.; Fu, R. W.; Tong, Y. X. *Langmuir* **2010**, *26*, 2209−2213.

(34) Fischer, A. E.; Pettigrew, K. A.; Rolison, D. R.; Stroud, R. M.; Long, J. W. *Nano Lett.* **2007**, *7*, 281−286.

(35) Fischer, A. E.; Saunders, M. P.; Pettigrew, K. A.; Rolison, D. R.; Long, J. W. *J. Electrochem. Soc.* **2008**, *155*, A246−A252.

(36) Shen, J.; Wang, J.; Zhai, J.; Guo, Y.; Wu, G.; Zhou, B.; Ni, X. *J. Sol−Gel Sci. Technol.* **2004**, *31*, 209−213.

(37) Wang, C. B.; Yin, L. W.; Xiang, D.; Qi, Y. X. *ACS Appl. Mater. Interfaces* **2012**, *4*, 1636−1642.

(38) Liu, N. N.; Yin, L. W.; Wang, C. X.; Zhang, L. Y.; Lun, N.; Xiang, D.; Qi, Y. X.; Gao, R. *Carbon* **2010**, *12*, 3759−3591.

(39) Zhou, W.; Cheng, C.; Liu, J. P.; Tay, Y. Y.; Jiang, J.; Jia, X. T.; Zhang, J. X.; Gong, H.; Hng, H. H.; Yu, T.; Fan, H. J. *Adv. Funct. Mater.* **2011**, *21*, 2439−2445.

(40) Chou, S. L.; Wang, J. Z.; Liu, H. K.; Dou, S. X. *J. Power Sources* **2008**, *182*, 359−364.

(41) Nanda, J.; Datta, M. K.; Remillard, J. T.; O'Neill, A.; Kumta, P. N. *Electrochem. Commun.* **2009**, *11*, 235−237.

(42) Fu, Z. W.; Wang, Y.; Zhang, Y.; Qin, Q. Z. *Solid State Ionics* **2004**, *170*, 105−109.

(43) Wang, L. M.; Liu, B.; Ran, S. H.; Huang, H. T.; Wang, X. F.; Liang, B.; Chen, D.; Shen, G. Z. *J. Mater. Chem.* **2012**, *22*, 23541−23546.

(44) Hsieh, C. T.; Lin, J. S.; Chen, Y. F.; Teng, H. S. *J. Phys. Chem. C* **2012**, *116*, 15251−15258.